

Design of surface acoustic wave resonators based on a series neural network

Cite as: Appl. Phys. Lett. **126**, 152201 (2025); doi: [10.1063/5.0251374](https://doi.org/10.1063/5.0251374)

Submitted: 2 December 2024 · Accepted: 3 April 2025 ·

Published Online: 15 April 2025



View Online



Export Citation



CrossMark

Fan Li,^{1,2} Yahui Tian,³ Lirong Qian,⁴ Zixiao Lu,¹ Qilong Chang,⁴ Haihang Xu,⁴ Guangwen Xiong,⁵ and Honglang Li^{1,a)}

AFFILIATIONS

¹National Center for Nanoscience and Technology, Beijing 100190, China

²University of Chinese Academy of Sciences, Beijing 100190, China

³Institute of Acoustics Chinese Academy of Sciences, Beijing 100190, China

⁴School of Integrated Circuit Science and Engineering, Tianjin University of Technology, Tianjin 300384, China

⁵Department of Letters & Science, University of Wisconsin-Madison, Madison, Wisconsin 53706, USA

^{a)}Author to whom correspondence should be addressed: lhl@nanoctr.cn

ABSTRACT

The surface acoustic wave (SAW) filter is widely applied in mobile communication, and the resonator is its main component. However, the traditional simulation and design methods of resonators often require much computation because the resonator includes a multilayer structure and many interfinger pairs. In order to improve the efficiency of simulation and designing, this paper proposed a series neural network to design the structural parameters backward based on the performance indicators. We validate the method using a SAW resonator based on a 42°YX cut LiTaO₃ substrate with an aluminum electrode. The device consists of an interdigital transducer and two reflector gates. The test set results from simulation data show that the trained model has a relative average error of less than 5% on the devices' structural parameters, and the coefficient of determination is more significant than 0.99. In addition, we compare the predicted and the experimental results, which show that the series neural network has excellent potential to infer the electrical response and structural parameters of SAW devices. The proposed method provides a potential solution for improving the efficiency of simulation and design of surface acoustic wave resonators.

Published under an exclusive license by AIP Publishing. <https://doi.org/10.1063/5.0251374>

Radio Frequency (RF) filters are essential in communication terminals such as base stations, mobile phones, and satellites. The RF filter mainly includes a capacitor, an inductor filter, a cavity filter, a low-temperature co-fired ceramic filter, an acoustic filter, and so on.¹ Since the speed of sound waves is five orders of magnitude slower than electromagnetic waves, acoustic filters can achieve smaller device sizes for easy integration. At present, acoustic filters mainly include surface and bulk acoustic wave filters; the former is relatively mature in theory and technology due to its early development.^{2–6}

The surface acoustic wave (SAW) filter comprises several resonators in series and parallel to filter the signal. Therefore, it is necessary to simulate and design the resonator before designing the filter.⁷ The simulation technology of the surface acoustic wave resonator consists of the equivalent circuit method,^{8–10} the coupled mode model,^{11–14} the finite element method,^{15–20} and the hierarchical cascade algorithm.^{21–26} The main indexes of evaluating simulation technology are simulation speed and accuracy. At present, the commonly used finite element method

and the hierarchical cascade algorithm developed based on the former achieve the highest accuracy compared with other methods, and the latter further improves the simulation speed based on the periodic structure of the SAW device. However, the simulation speed of such techniques is still ineffective for the device reverse design and optimization.

In recent years, researchers have begun to explore the simulation of surface acoustic wave resonators or the design of filters based on artificial intelligence (AI) technology, including machine learning and deep learning. The most significant advantage of this approach is that the trained model can give millisecond results for new simulation and design problems. There are two main categories of work of the previous researchers. One is combined with equivalent circuit or coupled mode models to assist traditional models with accuracy and ease of operation. For example, machine learning or deep learning methods can simulate the temperature-dependent behavior of the surface acoustic wave resonator,²⁷ establish the mapping relationship between the

SAW resonator structure parameters and the lumped parameters of the equivalent circuit model,²⁸ and predict the coupling mode model parameters based on the electrical curve.^{29,30} However, the limitation of this method is that it has little effect on improving the simulation speed. Another method takes the machine learning or deep learning model as an agent model, considering artificial intelligence-based technology to replace traditional simulation methods. For example, some studies use machine learning or deep learning methods to predict the electrical response parameters directly based on the structural parameters of SAW devices.³¹ However, this method skips the intermediate results of the electrical curve, and the prediction effect has room to continue to improve. In addition, combining a neural network agent and global optimization algorithm can design an SAW filter like the traditional design route, and the structural parameters are designed according to the performance requirements.^{32,33} However, the relationship between the structure of a single resonator and its electrical response curves is still lacking.

This paper presents a method based on a series of neural networks for further in-depth research of artificial intelligence technology in the SAW device design. This method plays the role of a neural network as an agent model instead of the traditional simulation method and realizes the end-to-end design of the device. Compared with previous studies, its unique advantage is that it provides a more detailed, rigorous, and predictive method for the design of SAW devices. Its distinction is establishing the mapping relationship among the three layers of the admittance curve, structure parameter, and input performance indicators. The previous studies using artificial intelligence methods as agent models have only analyzed the mapping between two layers. We also fully use the relationship between the performance indicators and the admittance curve to enhance the convergence of the

model based on Gaussian transformation. This study's significance and potential impact are to improve the application of artificial intelligence technology at the device level of SAW, establish a reasonable mapping model between each step, and provide more detailed and perfect guidance for applying artificial intelligence technology in the actual development and design. The admittance curve can be predicted based on input performance indicators, and the structure parameter can be predicted based on the admittance curve. We take 42°YX cut LiTaO₃ devices as an example, and the results of model training, testing, and experiments verify its potential.

The SAW resonator mainly comprises a piezoelectric substrate and an electrode layer, as shown in Fig. 1(a). The surface acoustic wave propagates on the surface of the piezoelectric substrate. It is excited by the electrical signal received by the interdigital electrode on the surface of the piezoelectric substrate. The piezoelectric coupled wave equation can describe the mathematical and physical model of the SAW resonator,

$$\epsilon_{ijkl}^E u_{k,li} + e_{kij} \phi_{,ki} - \rho u_{j,tt} = 0, \quad (1)$$

$$e_{ikl} u_{k,li} - \epsilon_{ik}^S \phi_{,ki} = 0. \quad (2)$$

Due to the large number of interfinger of SAW resonator, the calculation of the simulation of the whole model is extensive, so the model is generally simplified. Among them, the more simplified way is to take a wavelength as the period unit. X and Y directions need to set periodic boundary conditions. The bottom of the model sets a perfect match layer. The finite element method can calculate the SAW resonator's admittance curve and displacement field (vibration mode), as shown in Fig. 1(b).

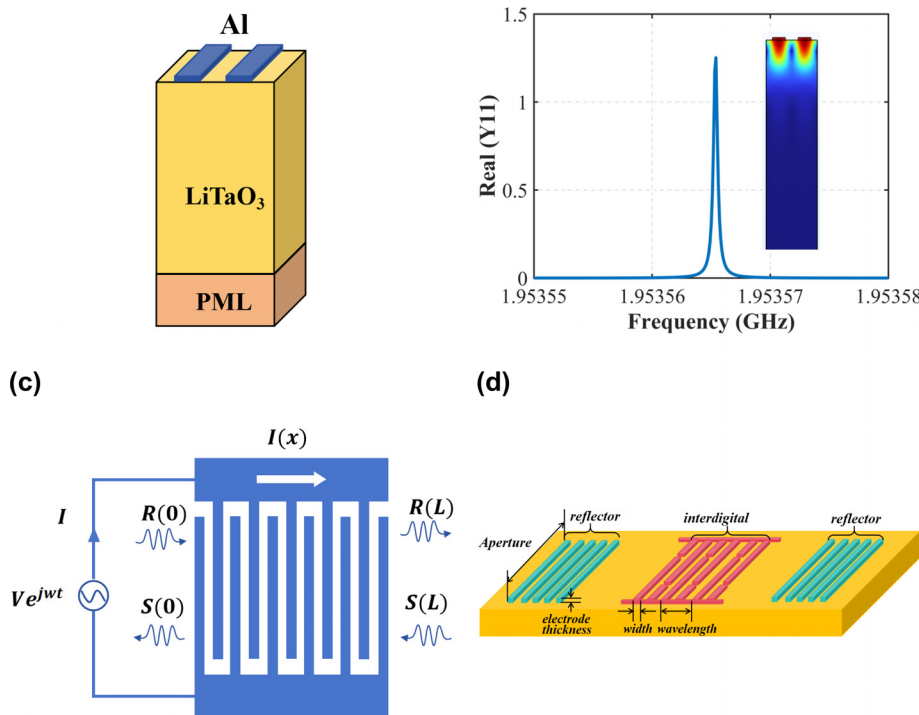


FIG. 1. (a) A single period unit of a SAW resonator. (b) Admittance curve and vibration modes of a surface acoustic wave resonator. (c) Diagram of coupling of mode; (d) structure of SAW resonator.

However, the finite element simulation of the device needs to divide many grids, which takes a long time. The coupling of mode (COM) model is a phenomenological model for SAW resonators, and the simulation speed is much faster than the finite element method. The coupled mode model mainly considers the transmission and reflection properties of the device to the sound wave and the admittance characteristics of the device between voltage and current. Figure 1(c) shows its principle. The COM model uses a set of equations to describe the acoustic and electrical behavior of SAW devices based on periodic disturbance theory [Eq. (3)]. Suppose the interdigital transducer (IDT) emission wave field and total current are the response, and the incident wave field and excitation voltage are the boundary conditions. In that case, we can use P-matrix to express the linear relationship [Eq. (4)]. P_{33} represents the device's admittance, and we can obtain the resonator's admittance characteristic by sweeping the device's frequency,

$$\begin{cases} \frac{dR(x)}{dx} = -j\delta R(x) + j\kappa S(x) + j\alpha V, \\ \frac{dS(x)}{dx} = -j\kappa^* R(x) + j\delta S(x) - j\alpha^* V, \\ \frac{dI(x)}{dx} = -j2\alpha^* R(x) - j2\alpha S(x) + jCwV, \end{cases} \quad (3)$$

$$\begin{bmatrix} \varphi_-(0) \\ \varphi_+(L) \\ I \end{bmatrix} = \begin{bmatrix} P_{11} & P_{12} & P_{13} \\ P_{21} & P_{22} & P_{23} \\ P_{31} & P_{32} & P_{33} \end{bmatrix} \begin{bmatrix} \varphi_+(0) \\ \varphi_-(L) \\ V \end{bmatrix}, \quad (4)$$

$$P_{33} = -\left[\frac{\alpha\delta + \alpha^*\kappa}{\delta^2 - |\kappa|^2} P_{31} + (-1)^N \frac{\alpha^*\delta + \alpha\kappa^*}{\delta^2 - |\kappa|^2} P_{32} \right] - 4Lj \frac{\delta |\alpha|^2 + \Re[\kappa^* \alpha^2]}{\delta^2 - |\kappa|^2} + j\omega CL. \quad (5)$$

The surface acoustic wave velocity v , reflection coefficient κ , energy exchange coefficient α , and capacitance C are parameters of the COM model, which vary with the device parameters. In order to extract COM parameters accurately, the upper and lower boundary frequencies of stop band in short circuit (f_{sc+} , f_{sc-}) and open circuit (f_{oc+} , f_{oc-}) are solved by the finite element method with solving characteristic frequency. Then, normalized electrostatic capacity is obtained based on a steady-state solution. Equations (6)–(9) show the extraction method of COM parameters,³⁴

$$v = \lambda \frac{f_{sc+} + f_{sc-}}{2}, \quad (6)$$

$$|\kappa|\lambda = 2\pi \frac{f_{sc+} - f_{sc-}}{f_{sc+} + f_{sc-}}, \quad (7)$$

$$|\alpha_n| = \sqrt{wC_n \lambda \pi \left(\frac{f_{oc+} + f_{oc-}}{f_{sc+} + f_{sc-}} - 1 \right)}, \quad (8)$$

$$C_n = \frac{2W_e}{(\Delta V)^2 W}. \quad (9)$$

In order to obtain the data needed for deep learning quickly, this paper generates the data set based on the COM model. The resonator parameters we consider include wavelength, electrode film thickness, metallization ratio, pairs of reflectors, interdigital, and aperture length.

TABLE I. Scanning range of structural parameters.

Structural parameter	Range
Wavelength (λ)	2.90–4.88 (μm)
Electrode thickness	6%–12% (λ)
Metallization ratio	0.4–0.7
Number of reflectors	10–50
Number of interdigital	20–100
Aperture length	10–50 (λ)

The metallization ratio is the ratio of electrode width and half wavelength. Figure 1(d) shows the specific parameters. Table I shows the parameter scanning information. The number of samples generated is 31 500. The design indicators used in this paper include five parameters: the starting frequency of admittance, stopping frequency, resonant frequency, peak value, and Q value. Figure 2 shows the calculation of the Q value. The constructed data set is divided into a 70% training set and a 30% test set to analyze the model's generalization performance.

The series neural network established in this paper consists of two neural network models. Figure 3 shows its framework. The purpose of the first neural network is to realize the mapping between the design index and the admittance curve, which is the real part of the curve used in this paper. Before training the neural network, data transformation is essential to accelerate the convergence rate. Standardization is a prevalent approach. Since the admittance curve is similar to the Gaussian function, this paper uses the Gaussian function to transform the input data. Compared with the traditional standardization method, the Gaussian transform helps improve the convergence of the network.

Equations (10) and (11) show the standardized and Gaussian transformations. The dataset size is m samples multiply n features. Standardization transforms the original data from the features perspective, and Gaussian transformation transforms the original data from the perspective of samples.

Standardization transformation

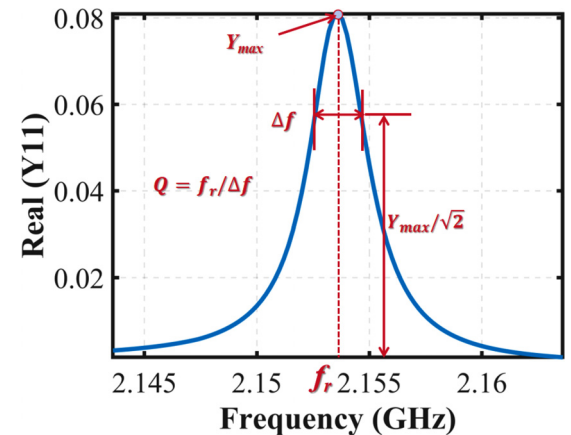


FIG. 2. Calculation method of the Q value.

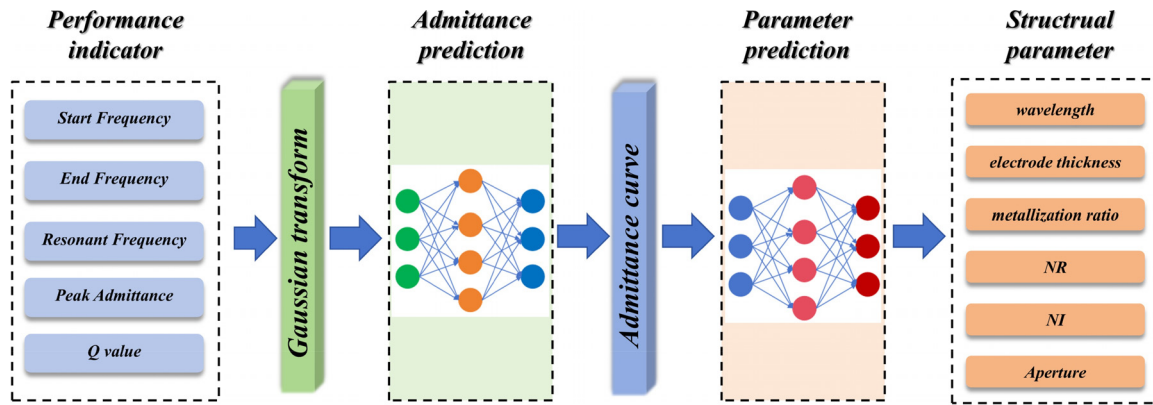


FIG. 3. Framework of series neural network for SAW resonator design.

$$Xtr_i = \frac{X_i - \mu_i}{\sigma_i} \quad (i, 2, \dots, n). \quad (10)$$

μ_i and σ_i represent the mean value and standard deviation of each feature, respectively.

Gauss transformation

$$Xtr_j = p_j \exp\left(-\frac{f_j - fr_j}{2c * \Delta f_j^2}\right). \quad (11)$$

p_j , fr_j , and Δf_j represent the admittance's peak value, resonant frequency, and frequency width, which correspond to half the peaks of

each sample, respectively. c is the correction factor that makes the fitting results more accurate.

The two models differ in addition to the output and output layers. Other structures remained the same. Its hyperparameters include the number of hidden layers, the number of hidden layer neurons, the activation function, and the optimizer. To determine the most suitable network architecture and hyperparameters, we scan and compare each hyperparameter of the model. The convergence trend is analyzed according to its loss curve. Figure 4 shows the results of the hyperparameter scanning.

Figure 4(a) shows that when the number of hidden layers is smaller, the convergence speed is faster since the network is simple and

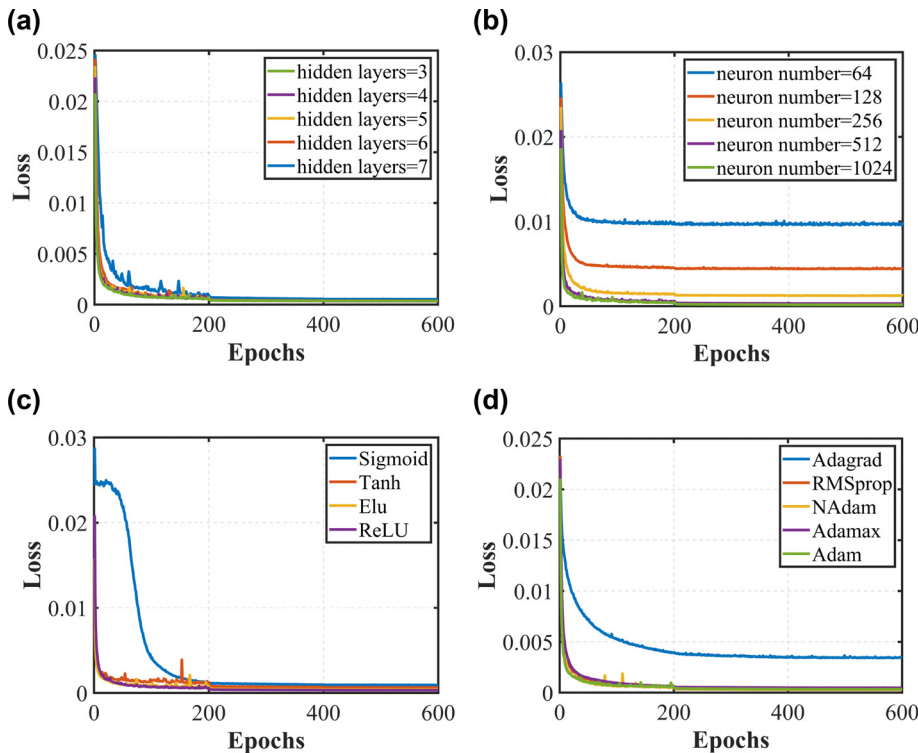


FIG. 4. Hyperparameter scanning and training loss plotting. (a) Number of hidden layers. (b) Number of hidden neurons per layer. (c) Activation function. (d) Optimizer.

TABLE II. Hyperparameters of neural network.

Model parameter	Value
Number of hidden layers	3
Number of neurons	512
Activation function	ReLU
Optimizer	Adam

the number of parameters is small. When the number of layers reaches three, the overall effect is close to stable. Figure 4(b) shows that when the number of hidden layer neurons is too small, the loss value of the final convergence of the network is higher since the neural networks are less expressive when the number of neurons is small. The final convergence value is stable when the number of neurons reaches 512 and above. Figure 4(c) compares the commonly used activation function types and shows that ReLU and Elu have faster convergence, while ReLU has a smoother convergence process. Figure 4(d) compares the commonly used neural network optimizers. Except for the poor convergence effect of Adagrad, the final convergence of other optimizers is close. Among them, the Adam optimizer converges faster in the early stage. Based on the overall analysis, the network hyperparameters were finally selected, as shown in Table II. In addition, we use piecewise learning to train the neural network for testing and subsequent training, which can achieve smooth convergence of the network. The piecewise learning rate is $[1 \times 10^{-3}, 1 \times 10^{-4}, 1 \times 10^{-5}]$.

Figure 5(a) shows the result of Gaussian fitting, which can capture the resonant frequency and resonance peak. The neural network needs to capture other details of the admittance curve further. Figure 5(b) shows the effect of standardization and Gaussian transformation on the network training process, where the data based on Gaussian transforms have significantly faster convergence and fewer minor final convergence errors. Figure 5(c) shows that the first network’s loss decreases to a convergence state.

The second neural network model aims to map admittance curves to structural parameters. Its training process is the same as that of the first neural network. Figure 5(d) shows that the second network’s loss decreases to a convergence state.

Figures 6–8 show the two-step prediction results of the series neural network. Figure 6 shows the predicted and simulated admittance curves have good fitting precision. Table III lists the indicators corresponding to the three sets of simulated and predicted admittance curves. Figure 7 shows the indicators of all sets of simulated and predicted admittance curves with a scatterplot. We use mean absolute percentage error (MPAE) and determination coefficient (R^2) to evaluate the performance of the second network. Equations (12) and (13) are the calculations of the two metrics. \hat{y}_i represents the i_{th} predicted sample. \bar{y}_i represents the mean value of actual samples. Results show that the indicators of simulated and predicted admittance curves are consistent. Figure 8 shows the prediction result of the second network model on the six structural parameters. The horizontal coordinate represents the actual device structure parameter, and the vertical coordinate represents the structure parameter predicted by the model according to

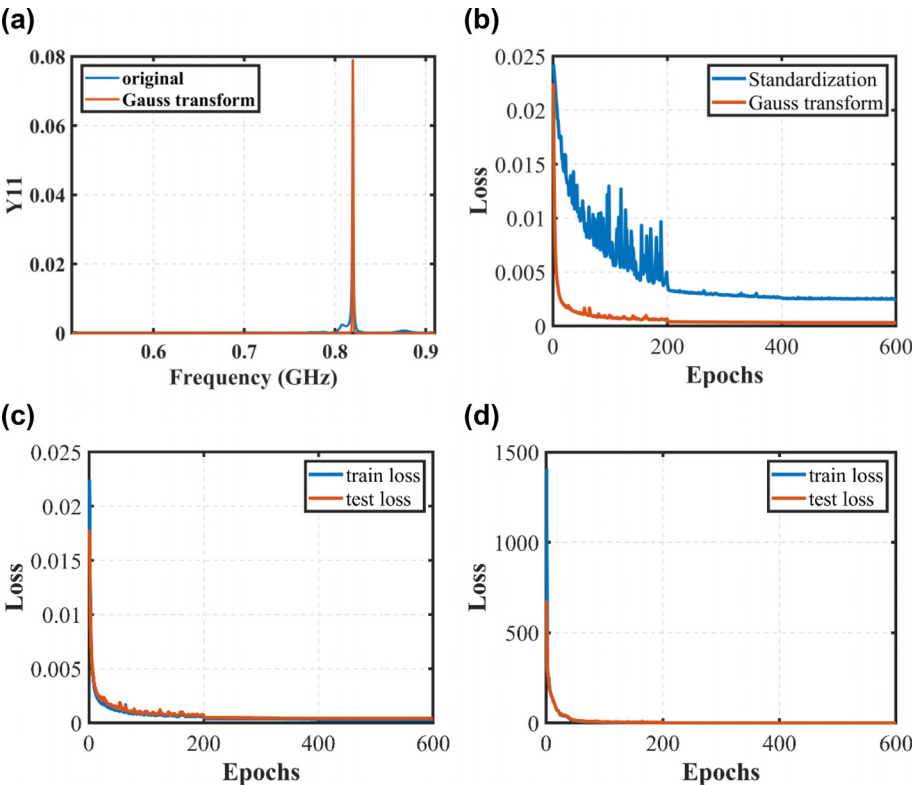


FIG. 5. (a) Comparison of original and transformed Y11. (b) Comparison of the effect on the convergence of standardization and Gauss transformation. (c) Train and test loss of the first neural network. (d) Train and test loss of the second neural network.

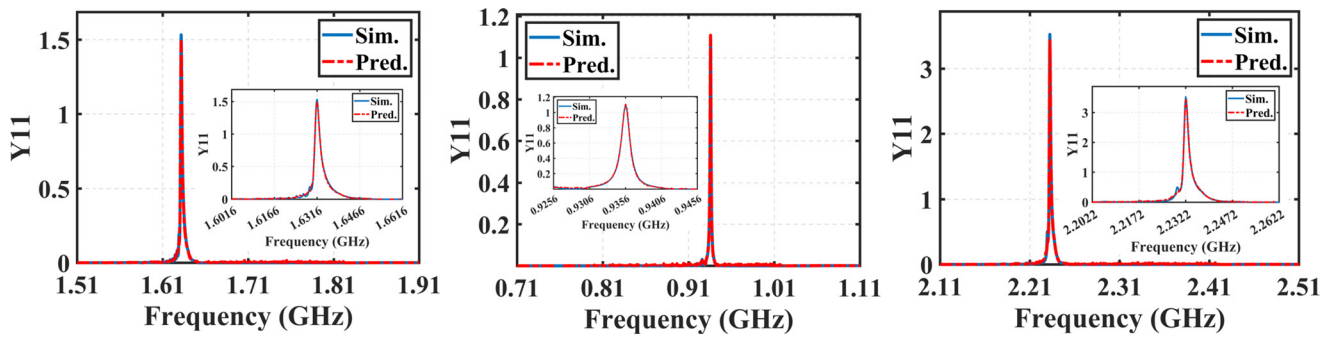


FIG. 6. Comparison of the predicted and simulated admittance curve based on the first neural network.

the admittance curve. The results show that the MAPE is less than 5%, and the R^2 is more significant than 0.99, which proves that the prediction has turned out well,

$$MAPE = \frac{1}{n} \sum_{i=1}^n \left| \frac{y_i - \hat{y}_i}{y_i} \right| \times 100\%, \quad (12)$$

$$R^2 = 1 - \frac{\sum_{i=1}^n (y_i - \hat{y}_i)^2}{\sum_{i=1}^n (y_i - \bar{y})^2}. \quad (13)$$

The advantage of this paper's series neural network model lies in establishing 3-part cascade mapping. In contrast, conventional machine learning methods generally directly establish the mapping between input indicators and predictive structural parameters. In order to verify the superiority of the proposed model, this paper sets five groups of controlled experiments. It uses conventional machine learning methods to predict structural parameters directly based on input indicators. Conventional machine learning methods we adopt include linear regression, Lasso regression, decision trees, random forests, and multilayer perceptrons. The evaluation and comparison were also conducted based on MAPE and R^2 metrics. Tables IV and V show the calculation results. The comparison results show that the series neural network based on two-step prediction has better accuracy than the conventional machine learning model based on input indicators and output parameters. The key reason the series neural network has this

effect is that the admittance curve has more information to predict the structural parameters, and the neural network can also extract information from the curve better.

In order to verify the accuracy of the proposed series neural network, we compared the experimental results of SAW resonators fabricated on the 42°YX cut LiTaO₃ substrate. The frequency of the resonator is in the range of 2–2.4 GHz. The device is fabricated through lithography and the liftoff process (Fig. 9). We obtain the SAW device's S parameters through a probe test and convert it to admittance. Figure 10 shows the experimental and predicted admittance curves based on a series neural network. The results show that our method effectively predicts the admittance curve's resonant frequency and peak value. Table VI records both input and calculation performance indicators from the predicted admittance curve and the experimental and actual structural parameters.

Now, we discuss the potential relationship between errors in predicting experimental results and parameter sensitivity. The resonant frequency is one of the most important indicators. Because the resonator is the basic unit that constitutes the filter, its resonant frequency determines the working band range of the filter. Its error is close to zero. The peak of the resonator's admittance determines the filter's final loss. Its measurement is easily affected by the impedance of other circuit components in the test equipment, and the error of sample testing and prediction is less than 10%, which belongs to the normal range. The calculation of the Q value is directly related to the point

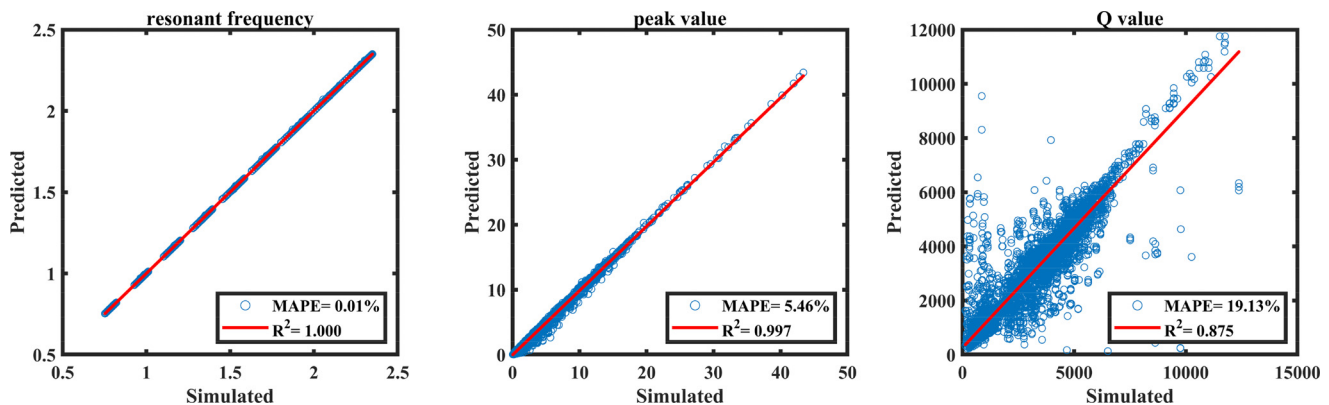


FIG. 7. Comparison of the indicators extracted from the simulated and predicted admittance curve based on the first neural network.

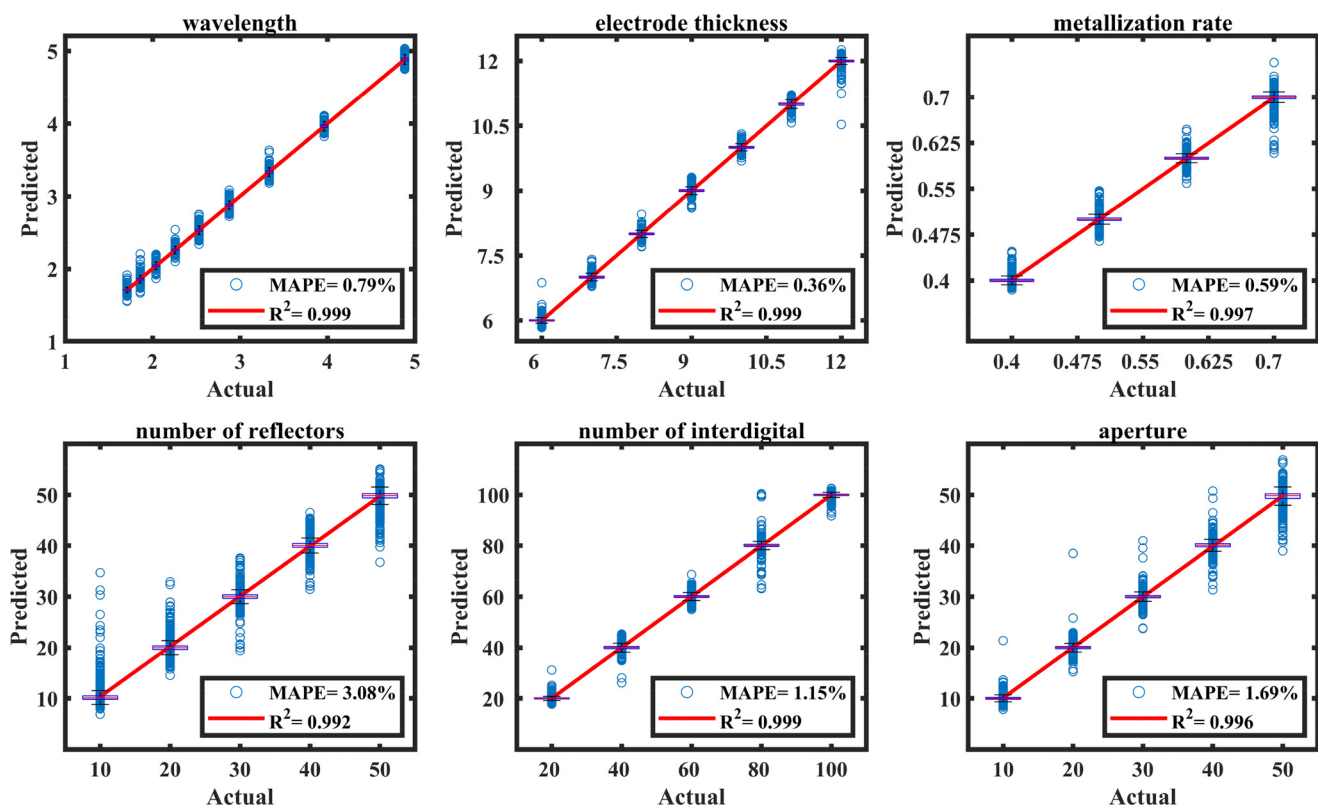


FIG. 8. Comparison of the predicted and actual structural parameters based on the second neural network.

density of the admittance curve and the overall trend of the curve. Its prediction difficulty is higher than the previous two, and the error is slightly larger. The wavelength of the device determines the resonant frequency of the device because its error is equivalent to the resonant frequency error. Metallization rate and electrode thickness determine the mass load of SAW devices and influence the peak admittance and Q value of SAW devices. The error is related to the error of peak admittance and Q value. The number and aperture size of the reflective gate and interdigital transducer (IDT) determine the distribution of

the metal layer, in which IDT is the source of energy excitation, so the number of IDT determines the device's overall performance. The prediction error of this parameter is relatively small, and the error of three samples is 10.34%, 7.27%, and 8.33%. The reflectors mainly reflect the acoustic wave, and the aperture mainly determines the transverse range of the acoustic wave. Both affect the acoustic performance of the device, and the effect is weakened when the number of reflective gates and the aperture width are enough. Therefore, it is reasonable that the two prediction errors are relatively large. The results prove that the framework captures key correlation principles and rules based on performance indicators, admittance curves, and structural parameters of SAW devices.

In conclusion, this paper proposed a series neural network framework for the surface acoustic wave device design. We analyze the influence of hyperparameters on the model and determine its optimal structure. The results of testing and verification on simulation data and experimental data show that the framework has a good prediction effect. Meanwhile, comparing it with the conventional machine learning method shows the superiority of step prediction. This work makes up for the shortcomings of the traditional machine learning prediction process based on indicators to performance parameters and realizes the end-to-end design of devices. It provides a valuable foundation for designing and applying AI technology in SAW devices in practical industrial applications. The method based on neural network has room for further improvement in the interpretability of the model. Future research can consider incorporating the physics equations of

TABLE III. Corresponding performance indicators of Fig. 6.

	Performance indicator	Resonant frequency	Peak value	Q value
No. 1	Simulated	1.6316	1.533 21	1171.89
	Predicted	1.6316	1.488 46	1070.39
	Error	0	2.91%	8.66%
No. 2	Simulated	0.9356	1.099 35	1025.67
	Predicted	0.9356	1.109 12	1016.75
	Error	0	0.89%	0.87%
No. 3	Simulated	2.2322	3.526 23	1923.93
	Predicted	2.2322	3.429 12	1788.26
	Error	0	2.75%	7.05%

TABLE IV. R^2 of conventional machine learning models and serial neural networks.

	Linear regression	Lasso regression	Decision tree	Random forest	Multilayer perceptron	Series neural network
Wavelength	0.914	0.914	0.924	0.978	0.999	0.999
Electrode thickness	0.871	0.856	0.762	0.883	0.978	0.999
Metallization rate	0.212	0.206	0.544	0.74	0.403	0.997
Number of reflectors	0.022	0.021	0.166	0.511	0.21	0.992
Number of interdigital	0.313	0.311	0.58	0.751	0.639	0.999
Aperture	0.226	0.227	0.229	0.546	0.387	0.996

TABLE V. MAPE of conventional machine learning models and serial neural networks.

	Linear regression	Lasso regression	Decision tree	Random forest	Multilayer perceptron	Series neural network
Wavelength	8.67%	8.68%	4.7%	3.1%	0.78%	0.79%
Electrode thickness	6.25%	6.62%	4.04%	4.67%	2.59%	0.36%
Metallization rate	15.18%	15.16%	5.71%	6.79%	12.37%	0.59%
Number of reflectors	40.51%	40.49%	28.18%	25.47%	35.15%	3.08%
Number of interdigital	32.44%	32.57%	18.1%	17.31%	22.98%	1.15%
Aperture	34.74%	34.77%	26.86%	23.86%	30.57%	1.69%

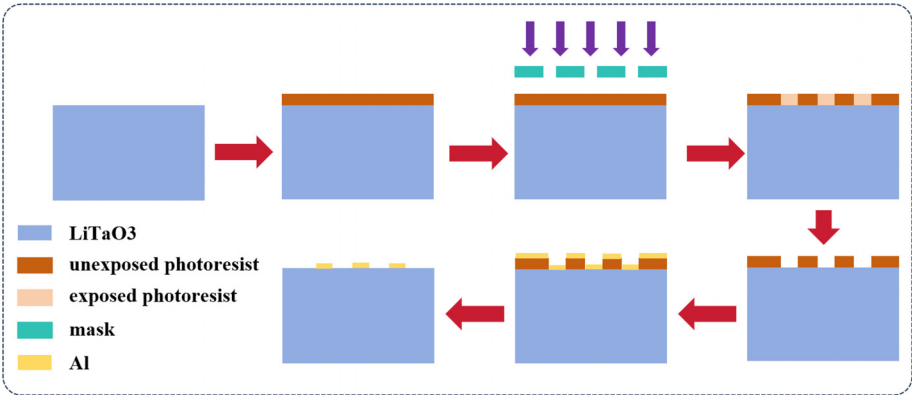


FIG. 9. Preparation process of SAW resonator.

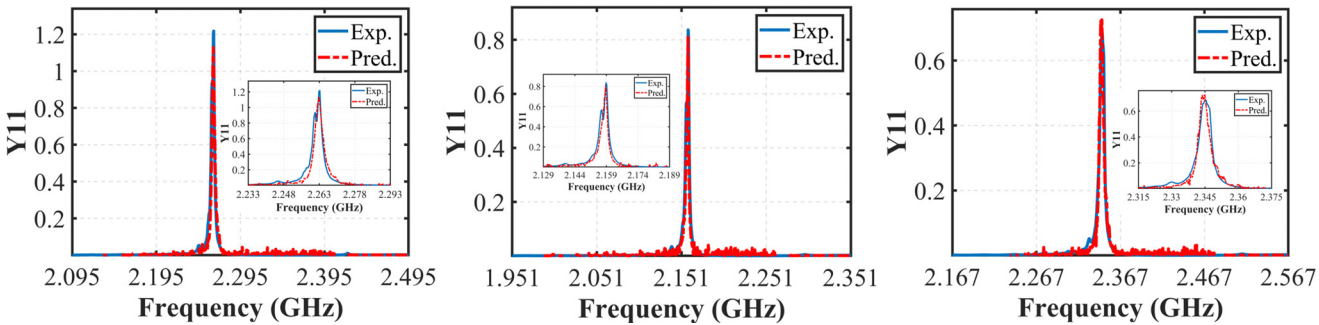


FIG. 10. Comparison of experimental and predicted admittance curve.

TABLE VI. Experimental and predicted indicators and structural parameter.

	Exp. 1	Pred. 1	Err. 1	Exp. 2	Pred. 2	Err. 2	Exp. 3	Pred. 3	Err. 3
Resonant frequency	2.2632	2.2628	0.02%	2.1588	2.1586	0.01%	2.3451	2.3449	0.01%
Peak value	1.2175	1.1283	7.3%	0.8367	0.8096	3.24%	0.689	0.7251	5.24%
Q value	750.25	909.31	21.2%	1383.6	1293.9	6.48%	689.29	772.15	12.02%
Wavelength	1.72	1.72	0	1.82	1.8	1.10%	1.67	1.72	2.99%
Electrode thickness	8.5	8.479	0.25%	8	8.772	9.65%	8.75	8.314	4.98%
Metallization ratio	0.47	0.478	1.7%	0.495	0.52	5.05%	0.495	0.479	3.23%
Number of reflectors	58	18	68.97%	55	70	27.27%	60	49	18.33%
Number of interdigital	58	64	10.34%	55	59	7.27%	60	55	8.33%
Aperture length	18.02	9.31	48.34%	33.4	23.78	28.80%	36.53	31.07	14.95%

the device working principle into the construction of neural networks, which will help improve the model’s precision and generalization.

This work was supported by the National Key Research and Development Program of China (Nos. 2022YFA1204602 and 2022YFB3606702). Additional support is through Beijing Nova Program (No. 20220484172), the Key Research Project of Guangdong Province (No. 2023B0101190002), Youth Innovation Promotion Association, Chinese Academy of Sciences (Grant No. 2022024), and Open project of the National Key Laboratory (No. JCKYS2023604SSJS002). This work was also supported by the China Institute of IoT and WuXi IOT Innovation Promotion Center.

AUTHOR DECLARATIONS

Conflict of Interest

The authors have no conflicts to disclose.

Author Contributions

Fan Li: Data curation (lead); Formal analysis (lead); Investigation (lead); Methodology (lead); Writing – original draft (lead). **Yahui Tian:** Writing – review & editing (equal). **Lirong Qian:** Writing – review & editing (equal). **Zixiao Lu:** Funding acquisition (equal). **Qilong Chang:** Data curation (equal). **Haihang Xu:** Data curation (equal). **Guangwen Xiong:** Resources (equal). **Honglang Li:** Writing – review & editing (equal).

DATA AVAILABILITY

The data that support the findings of this study are available from the corresponding author upon reasonable request.

REFERENCES

¹K. Yang, C. G. He, J. M. Fang, X. H. Cui, H. D. Sun, Y. S. Yang, and C. J. Zuo, *Chip* **2**(4), 100058 (2023).
²P. Chen, G. Li, and Z. Zhu, *Micromachines* **13**(5), 656 (2022).
³B. K. Turuk and B. Behera, *Eng. Res. Express* **6**(2), 022302 (2024).
⁴P. Delsing, A. N. Cleland, M. J. A. Schuetz, J. Knoerzer, G. Giedke, J. I. Cirac, K. Srinivasan, M. Wu, K. C. Balram, C. Bauerle, T. Meunier, C. J. B. Ford, P. V. Santos, E. Cerdá-Mendez, H. Wang, H. J. Krenner, E. D. S. Nysten, M. Weiss, G. R. Nash, L. Thevenard, C. Gourdon, P. Rovillain, M. Marangolo, J.-Y.

Duquesne, G. Fischerauer, W. Ruile, A. Reiner, B. Paschke, D. Denysenko, D. Volkmer, A. Wixforth, H. Bruus, M. Wiklund, J. Reboud, J. M. Cooper, Y. Fu, M. S. Brugger, F. Rehfeldt, and C. Westerhausen, *J. Phys. D: Appl. Phys.* **52**(35), 353001 (2019).
⁵Y. Yang, C. Dejos, and H. Hallil, *Micromachines* **14**(1), 43 (2023).
⁶J. Zhou, Y. Guo, Y. Wang, Z. Ji, Q. Zhang, F. Zhuo, J. Luo, R. Tao, J. Xie, J. Reboud, G. McHale, S. Dong, J. Luo, H. Duan, and Y. Fu, *Appl. Phys. Rev.* **10**(2), 021311 (2023).
⁷C. C. W. Ruppel, *IEEE Trans. Ultrason. Ferroelectr. Freq. Control* **64**(9), 1390–1400 (2017).
⁸T. Kojima and H. Obara, *Ferroelectrics* **241**(1–4), 215–222 (2000).
⁹T. Kojima and K. Shibayama, *Jpn. J. Appl. Phys.* **24**, 142–144 (1985).
¹⁰J. Munshi and S. Tuli, *IEEE Trans. Ultrason. Ferroelectr. Freq. Control* **51**(7), 783–785 (2004).
¹¹Y. Y. Chen, T. T. Wu, and T. T. Chou, *J. Phys. D: Appl. Phys.* **37**(1), 120–127 (2004).
¹²X. Jiang, Y. Shi, H. L. Wang, B. L. Zhao, and B. Du, “Design of low loss surface acoustic wave filter with three interdigital transducers,” in *2008 Symposium on Piezoelectricity, Acoustic Waves, and Device Applications* (IEEE, 2008), pp. 300–303.
¹³H. F. Li, R. Jia, W. L. Li, C. Chen, and X. Y. Liu, *J. Nanosci. Nanotechnol.* **10**(11), 7258–7261 (2010).
¹⁴Y. L. Zou, X. Y. Yang, P. Luo, and Y. H. Liu, *Micromachines* **15**(5), 664 (2024).
¹⁵A. S. Koigerov, *Opt. Spectrosc.* **132**(1), 54–63 (2024).
¹⁶M. Li, X. Xia, K. Li, S. Wu, J. Zou, K. Chen, and G. Tang, *IEEE Electron Device Lett.* **43**(10), 1772–1775 (2022).
¹⁷Q. Li, S. L. Fu, Z. T. Lu, L. R. Qian, R. Wang, T. J. Chen, C. Song, F. Zeng, W. B. Wang, and F. Pan, *Curr. Appl. Phys.* **19**(4), 363–369 (2019).
¹⁸J. Shen, S. Fu, R. Su, H. Xu, Z. Lu, Z. Xu, J. Luo, F. Zeng, C. Song, W. Wang, and F. Pan, *IEEE Trans. Microwave Theory Tech.* **69**(8), 3693–3705 (2021).
¹⁹P. Ventura, J. M. Hodé, M. Solal, J. Desbois, and J. Ribbe, in *1998 IEEE Ultrasonics Symposium - Proceedings* (IEEE, 1998), Vols. 1 and 2, pp. 175–186.
²⁰G. S. Xu and Q. Jiang, *J. Intell. Mater. Syst. Struct.* **12**(2), 69–77 (2001).
²¹Z. Chen, Q. Zhang, S. Fu, X. Wang, X. Qiu, and H. Wu, *Micromachines* **12**(1), 5 (2021).
²²Y. L. Huang, J. F. Bao, X. Y. Li, B. F. Zhang, L. Y. Qiu, T. Omori, and K. Y. Hashimoto, *IEEE Trans. Ultrason. Ferroelectr. Freq. Control* **66**(7), 1255–1263 (2019).
²³J. Koskela, V. Plessky, P. Maniadi, P. Turner, B. Willemsen, and IEEE, in *2017 IEEE MTT-S International Microwave Symposium (IMS)* (IEEE, 2017), pp. 1480–1482.
²⁴J. Koskela, V. Plessky, B. Willemsen, P. Turner, B. Hammond, and N. Fenzi, *IEEE Trans. Ultrason. Ferroelectr. Freq. Control* **65**(10), 1933–1942 (2018).
²⁵N. Matsuoka, L. Qiu, X. Li, T. Omori, and K.-Y. Hashimoto, *Jpn. J. Appl. Phys.* **58**, SKK12 (2019).
²⁶R. X. Su, J. Y. Shen, Z. T. Lu, H. P. Xu, Q. S. Niu, Z. B. Xu, F. Zeng, C. Song, W. B. Wang, S. L. Fu, and F. Pan, *IEEE Electron Device Lett.* **42**(3), 438–441 (2021).
²⁷M. Radojkovic, G. Gugliandolo, M. Latino, Z. Marinkovic, G. Crupi, and N. Donato, *Micromachines* **14**(5), 967 (2023).

- ²⁸M.-H. Chung, H.-C. Huang, R.-C. Hwang, P.-F. Huang, and S. T. Wang, *Sens. Mater.* **31**(7), 2225–2236 (2019).
- ²⁹X. Li, Z. Ji, J. Zhou, Y. Guo, Y. He, J. Zhang, and Y. Fu, *Sens. Actuators, A* **369**, 115158 (2024).
- ³⁰Y. Yang, A. Loseu, C. Zheng, W. Ni, W. Xu, R. Hong, Q. Liu, and IEEE, in *2024 IEEE MTT-S International Conference on Microwave Acoustics & Mechanics, IC-MAM* (IEEE, 2024), pp. 85–88.
- ³¹Y. B. Chu and Y. Zhang, *Energy Rep.* **8**, 90–97 (2022).
- ³²X. Hou, H.-J. Hu, L.-Y. Xiao, K. Chen, M. Zhuang, and Q. H. Liu, in *2024 IEEE MTT-S International Conference on Microwave Acoustics & Mechanics, IC-MAM* (IEEE, 2024), pp. 57–60.
- ³³X. Hou, H.-J. Hu, L.-Y. Xiao, K. Chen, M. Zhuang, and Q. H. Liu, *IEEE Sens. J.* **24**(16), 26971–26981 (2024).
- ³⁴X. Ma, H. Lei, P. Cai, and X. Ji, *Appl. Sci.* **12**(9), 4547 (2022).